

PAPER

Underwater hyperspectral imaging bioinspired by chromatic blur vision

To cite this article: Tiantian Chen *et al* 2023 *Bioinspir. Biomim.* **18** 016015

View the [article online](#) for updates and enhancements.

You may also like

- [Adaptive and automatic red blood cell counting method based on microscopic hyperspectral imaging technology](#)
Xi Liu, Mei Zhou, Song Qiu et al.
- [A low-rank estimation method for CTIS image reconstruction](#)
Qifeng Li, Yang Wang, Xiangyun Ma et al.
- [Intraoperative hyperspectral label-free imaging: from system design to first-in-patient translation](#)
Michael Ebner, Eli Nabavi, Jonathan Shapey et al.

Bioinspiration & Biomimetics



PAPER

Underwater hyperspectral imaging bioinspired by chromatic blur vision

Tiantian Chen¹ , Jiarui Zhao¹ , Yunzhuo Liu¹ and Shuyue Zhan^{1,2,*}

¹ Ocean College, Zhejiang University, Zhoushan 316021, People's Republic of China

² Key Laboratory of Ocean Observation-Imaging Testbed of Zhejiang Province, Zhejiang University, Zhoushan 316021, People's Republic of China

* Author to whom any correspondence should be addressed.

E-mail: shuyue_zhan@zju.edu.cn

Keywords: vision bionics, underwater hyperspectral imaging, chromatic blur, image reconstruction

Supplementary material for this article is available [online](#)

Abstract

In the underwater environment, conventional hyperspectral imagers for imaging target scenes usually require stable carrying platforms for completing push sweep or complex optical components for beam splitting in long gaze imaging, which limits the system's efficiency. In this paper, we put forward a novel underwater hyperspectral imaging (UHI) system inspired by the visual features of typical cephalopods. We designed a visual bionic lens which enlarged the chromatic blur effect to further ensure that the system obtained blur images with high discrimination of different bands. Then, chromatic blur datasets were collected underwater to complete network training for hyperspectral image reconstruction. Based on the trained model, our system only required three frames of chromatic blur images as input to effectively reconstruct spectral images of 30 bands in the working light range from 430 nm to 720 nm. The results showed that the proposed hyperspectral imaging system exhibited good spectral imaging potential. Moreover, compared with the traditional gaze imaging, when obtaining similar hyperspectral images, the data sampling rate in the proposed system was reduced by 90%, and the exposure time of required images was only about 2.1 ms, reduced by 99.98%, which can greatly expand its practical application range. This experimental study illustrates the potential of chromatic blur vision for UHI, which can provide rapid response in the recognition task of some underwater dynamic scenarios.

1. Introduction

Hyperspectral imaging is a technique for acquiring images in continuous narrow bands, which can be used to analyze the 'spectral fingerprint' and spatial distribution of large-scale detection objects [1, 2]. It is widely used in satellite remote sensing [3], biomedical imaging [4, 5], water contamination analysis [6] and other fields [7, 8]. Its characteristic of high spectral resolution is not available in other types of photoelectric imaging [1–3, 9, 10]. However, this imaging modality typically requires a spatial translational push sweep or a long gaze (during the scanning wavelength), to obtain the hyperspectral image of a scene. Both of these need to rely on a more stable carrying platform, limiting the application of hyperspectral imaging technology to some extent

[11–13]. Dumke *et al* designed a push-broom underwater hyperspectral imaging (UHI) prototype, realizing the spectroscopic imaging of two hydrothermal SMS mounds in the TAG hydrothermal field at the Mid-Atlantic Ridge [14]. Xue *et al* developed a UHI system of prism-grating-prism structure and carried out testing experiments in the lab with ColorChecker 24 as the target [15]. The results indicated its high stability as well as imaging quality. However, the data acquisition for both the above UHI systems needed a bulky mounting platform with necessary push-broom structure. Moreover, these scanning devices and platforms complicate the overall mechanical structure required in imaging. In addition, there exist other spectral imaging techniques that can be implemented by setting up a tunable light source [16] or using a liquid crystal tunable filter (LCTF) [17].

These methods need to snap images of each switched band separately to complete spectral imaging for a scene, resulting in a long time and high cost for hyperspectral imaging of a single scene. In response to these problems, bioinspired by the vision of cephalopods, the technique of UHI was studied herein from the perspective of bionic vision.

Cephalopods, such as octopus and squid, have long been considered the most colorful creatures in the ocean. They are known as 'experts in color change and camouflage'. Some bio-physiological studies [18–21] suggest that the retina of cephalopod contains single photoreceptor (which can sense about 400 nm–600 nm of visible light), meaning that they are color-blind. The phenomenon of color-blind animals being able to transmit and conduct information inside and camouflage through skin discoloration has attracted the interest of many scholars, but the visual perception mechanism has not been revealed clearly. Jagger and Sands [22, 23] studied the eyeball optical system of squid, and pointed out that its eyeball has features such as large aperture, short focal length and gradual refractive index. These features are conducive to increasing the light transmittance and improving the brightness of the retinal image, and adapting to life in a low light environment underwater. However, its optical system has an unrectified axial chromatic aberration, with a focal length offset of about 0.75 mm in the visible band range of 400 nm–700 nm. Based on the previous studies [17, 20], Stubbs and Stubbs [24] further found that the epiretinal imaging has a large vertical axis chromatic aberration, namely blur defocused images, due to the high axial chromatic deviation of the eyeball optical system and the large aperture or off-axis pupil characteristics. Thus, they believed that squids may adjust the accommodation between the eyeball and the retina to obtain a series of chromatic blur images at the axial position on the retina, and approximately perceive various reflected spectral components of the target object through the image contrast analysis of each frame. However, this visual mechanism requires a target with a sharp contrasting structure to the background, which may show low perceptual efficiency when two adjacent targets have similar color or spectral reflection, and fails to explain how spatial resolution can be obtained.

Although the squid visual perception mechanism is still not clear, a bionic hyperspectral imaging idea was put forward by our group: first, bionic design an imaging lens with high chromatic aberration based on the optical properties of the squid eyeball, which can obtain the chromatic blur image of scene object. Then, recover clear hyperspectral image through digital image processing or convolutional neural network (CNN) algorithm. Previously, the feasibility of the concept was verified through simulation model as well as numerical calculation. Singular value decomposition, Jansson-van Cittert algorithms

and other deconvolution algorithms were successfully used to restore the chromatic blur images and restore the spectral images in each band [25, 26]. The results demonstrated the availability of any region's spectra in the target as well as clear spatial resolution. However, such traditional deconvolution algorithms require chromatic blur images of full-band focused position as input, which requires the imaging system to spend some time in gaze scanning and limits its application in complex environmental conditions such as underwater. In contrast, CNN for deep learning is better suited for hyperspectral image reconstruction for such high-dimensional and super-resolution tasks [27–29].

Here, a first prototype of bionic spectral imaging system based on squid visual mechanism for underwater spectral imaging in relatively clear waters was presented. This system featured chromatic blur, which means the imaging blur is basically due to chromatic aberration. By calibrating the chromatic blur curve, the focal position of each frame can be determined to form the dataset. For pixel-level reconstruction of hyperspectral images, the CNN method was selected, whose structure was further designed to achieve a faster spectral imaging performance of large-scale images. The experimental results show that 30 bands of spectral images can be effectively obtained based on the trained model, and UHI based on chromatic blur bionic vision was realized.

2. Chromatic blur lens and imaging system design

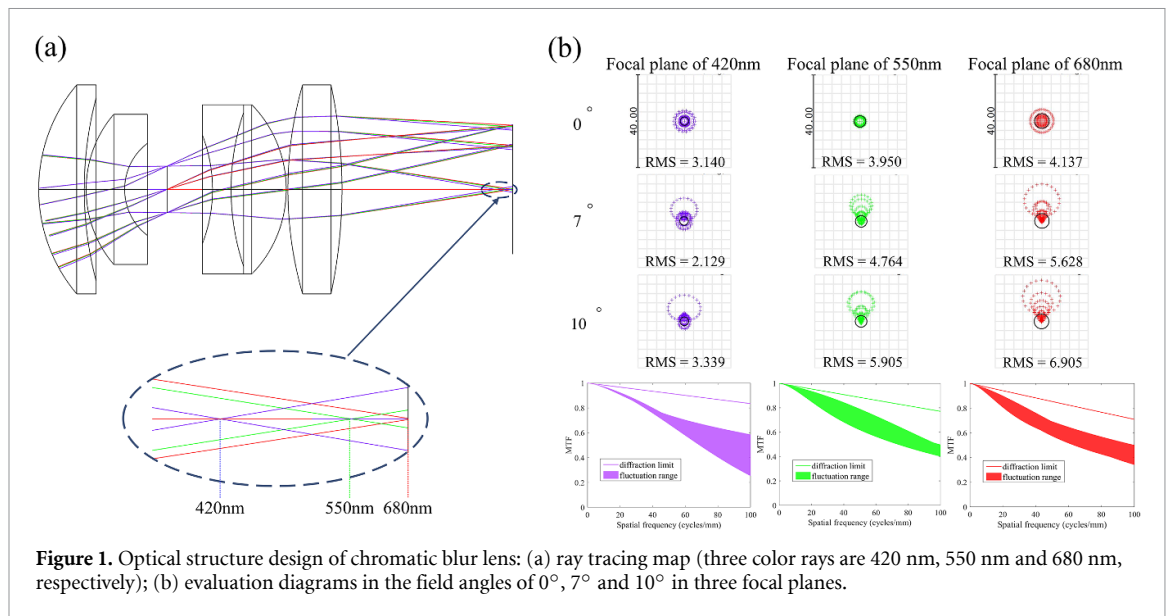
2.1. Lens design

The squid eye medium has a gradual refractive index feature, which greatly increases the transmitted light and corrects the remaining aberrations outside of the chromatic aberration [24]. Inspired by this characteristic, a lens with high chromatic aberration was designed following the requirements below:

- (a) The working bands cover the visible light region, and all parts of the lens are compact;
- (b) Axial chromatic aberration with a large and monotonic variation;
- (c) Monochromatic aberrations are corrected except chromatic aberration.

The overall lens' design was completed using ZEMAX software. Considering the requirement c, a double Gaussian objective lens in ZEMAX was selected as the initial structure which featured little initial aberrations and then its focal length was scaled. In the visible light range, 420 nm, 550 nm and 680 nm were selected as the three reference incident wavelengths, and three configurations were set accordingly assigning various weights to each wavelength.

During the optimization stage, unlike the case with ordinary imaging lenses, the chromatic



aberration of the proposed system needs to be preserved. Therefore, some evaluation methods such as wave aberration and modulation transfer function (MTF) are not suitable. Instead, an evaluation criterion of spot radius was used, the parameters of curvature radius, glass thickness, and air interval of each lens were set as variables, and the glass material was changed into a replacement state. Some necessary operands such as DIST, LONA, AXCL, etc were used to reduce the unwanted aberrations and ensure a large chromatic dispersion scale. After a series of optimizations, manually as well as automatically, the final lens model was obtained, as shown in figure 1, including the overall structure and image quality evaluation.

The model consists of four lenses and a large circular aperture between the second and third one, with a theoretical focal length of 30.433 mm at 550 nm wavelength. The chromatic focal shift of the lens in the range from 420 nm to 680 nm is 2.369 mm, as shown in figure 1(a). In addition, its imaging quality was also evaluated through spot diagrams and MTF curves in three focal planes. The smaller the root mean square (RMS) value, the more concentrated the energy of the incident light. Only the energy concentration of corresponding wavelength on each focal plane needs to be ensured, considering the specific characteristic of the proposed chromatic lens. The values shown in figure 1(b) are almost within six, which meets the pixel size of most scientific cameras. In addition, MTF characterizes the ability to resolve images. In general, its value at half the Nyquist frequency is significant [30]; the closer it is to the diffraction limit, the better the imaging quality is, indicating higher imaging contrast. MTF diagrams in three focal planes are also shown in figure 1(b), where the lines represent the corresponding diffraction limit while the colored areas denote MTF fluctuation ranges of the lens in three field angles of 0°, 7°

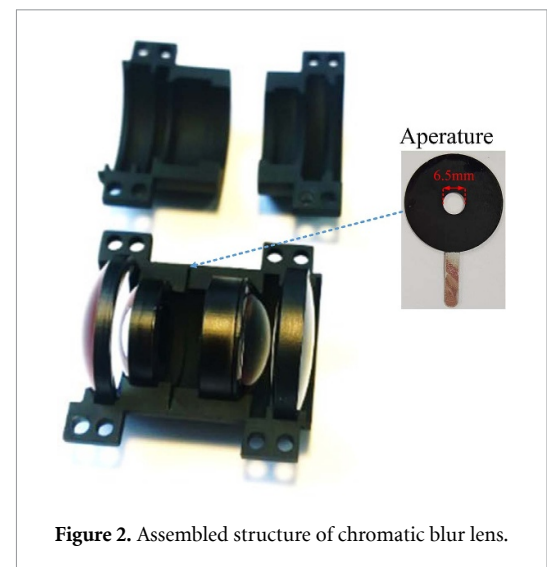


Figure 2. Assembled structure of chromatic blur lens.

and 10°. The Nyquist frequency of the camera used in subsequent experiments (with pixel pitch of $5.04 \mu\text{m}$) is $99.2 \text{ cycles mm}^{-1}$ and the mid-frequency MTFs are all above 0.6, indicating high imaging quality on the whole.

Figure 2 shows the solid structure of the proposed chromatic blur lens and the blacked stainless-steel aperture with an inner aperture of 6.5 mm. The third part in the lens is a double adhesive lens with Canadian gum glue. To avoid the stray light crosstalk and improve the light energy transmittance, the incident emission surface of each lens with a maximum reflectivity of 0.5% (380 nm–820 nm) was coated, and black paint was applied on the side and the aperture surface. The mechanical structure of the lens cylinder was designed according to the lens optical design model, and it was printed out by 3D technique using fine-surfaced photosensitive resin 9400 material. The lenses were exactly embedded into the lens

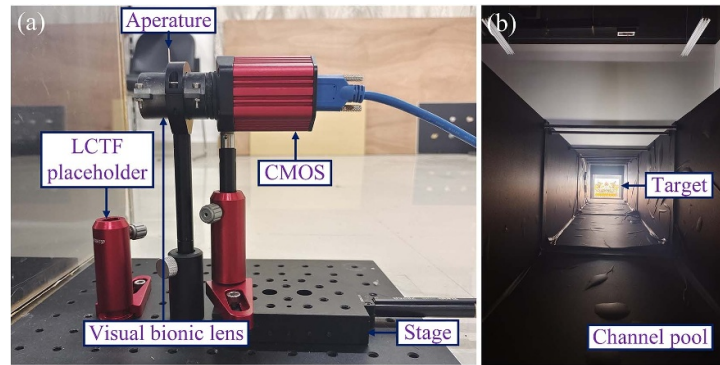


Figure 3. Experiment setup: (a) chromatic blur imaging system; (b) experimental subject through an acrylic tank with blackened interior.

cylinder and the final assembled specification size was $\Phi 35 \text{ mm} \times 45 \text{ mm}$.

2.2. Imaging system setup

A chromatic blur imaging system (figure 3(a)) was built on optical plates. A scientific complementary-metal-oxide-semiconductor (sCMOS) monochromatic camera (Thorlabs, CS2100M) was used and fixed to the electronic control displacement table (Thorlabs, PT1-Z8) to complete the chromatic blur image acquisition by axial scanning motion precisely. In addition, spectral images of the scene object were also collected during the process, which served as labels for later network training and alignment verification of network reconstruction results. Thus, the LCTF (CRI, VIS-10-20 VariSpec Filter) was installed for assisting in spectral images shooting. Specifically, the LCTF was made to work at a certain wavelength and the camera was moved to the focus position of the wavelength to catch a corresponding quasi-spectroscopic image.

2.3. Underwater target imaging environment

As shown in figure 3(b), an acrylic plate was used to build a tank container. The imaging detection end surface was illuminated, and the overall size of the tank was $0.6 \text{ m} \times 0.6 \text{ m} \times 5 \text{ m}$ with inner surface blackened. The imaging target was mainly printed with a series of color pictures and placed at one end of the tank. Four 35 W waterproof light-emitting diode (LED) lights were used as lighting sources for the target, which were installed around the target in a luminous wavelength range of 430 nm–720 nm. The imaging system was placed outside the other transparent end of the tank relative to the target, and the final actual imaging distance was 5.05 m. Moreover, the internal blackening-processed acrylic box hood was used outside the imaging system device and a light window was opened at the front end of the box to reduce stray light effects.

3. Calibration experiment and modeling

3.1. System calibration

3.1.1. Chromatic aberration calibration

Due to the monotonically varying high chromatic property of the proposed imaging lens, various incident wavelengths from object have different image axial focusing positions. The relationship between the wavelength and the axial focusing position constitutes the chromatic aberration curve. From the lens model of ZEMAX, a theoretical chromatic aberration curve can be obtained (expressed in the form of relative displacement from a certain wavelength focus surface). However, once the system has been built, the motion working position of the electro-controlled displacement station at different wavelengths should be determined to obtain the corresponding image. Therefore, the chromatic aberration curve should be actually measured, whose ordinate values indicate the focal plane, which means the clearest imaging position.

The general method of identifying the optimum focusing position is to combine USAF-1951 or ISO 12233 resolution test target with the evaluation of MTF, which is not very effective for the proposed chromatic blur system. Specifically, the actual effect is limited by the long imaging distance of beyond 5 m and the hard choice of properly selecting a solvable region to calculate MTF in the proposed system, resulting in undesirable disturbance in the generated curve. Hence, a standard aluminum-oxide coated calibration plate featuring 12×9 checkerboard pattern (GP400- 12×9 , $40 \text{ cm} \times 30 \text{ cm}$) was used as the target object (as shown in the sub-diagram of figure 4), and the medium in the sink was air. The LCTF was installed in front of the imaging system lens to switch the narrow-band transmission wavelength dividing from the target reflected light radiation. When LCTF set a certain light transmission wavelength, the electrical displacement stage moved by 0.01 mm, and the chromatic blur image was collected each time.

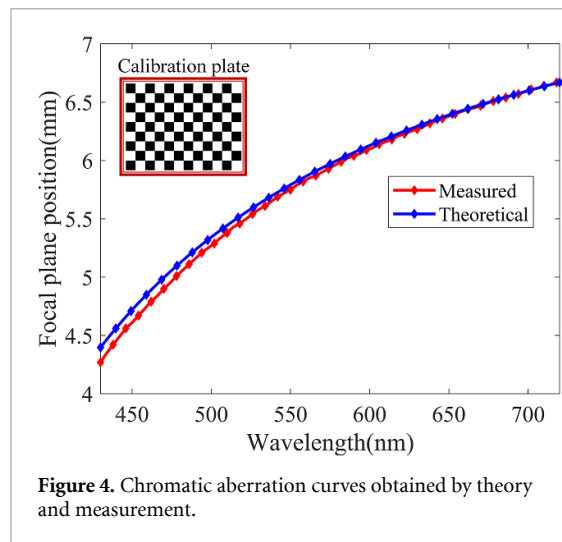


Figure 4. Chromatic aberration curves obtained by theory and measurement.

The frame with clearest edges in this batch was chosen as the focus spectral image at this wavelength, and the position of the displacement stage was the focus position of the wavelength. During the process, image clarity evaluation was implemented by edge detection using Tenengrad gradient method based on the Sobel operator [31]. This work was performed automatically by writing a control script to traverse all the needed working wavelengths, analyze the location of the clearest image, and complete the actual measurement of the objective chromatic aberration curve. Moreover, the measured curve was compared with the theoretical chromatic aberration curve (figure 4) derived from ZEMAX, by aligning the two at the focus position of 720 nm. The RMS value was 0.0562, which confirmed that the proposed physical lens and the theoretical model are highly matched in the axial chromatic aberration characteristics.

3.1.2. Radiance calibration

Hyperspectral imaging is typically applied to measure the optical properties of the analyzed scene objects such as the spoke luminance, reflectivity, etc. Calibration is necessary to establish the correspondence between the digital image pixel value and the optical physical amount. Referring to the comparative contrast method [32] used by Nguyen, a standard diffuse whiteboard (Jingyi optoelectronics, 50 cm × 50 cm) was used as the target to capture its spectral images according to the calibrated chromatic aberration curve under the same experimental conditions. Then, a region of interest (ROI) in the whiteboard was measured by spectral brightness analyzer (Hopoo-color, OHSP-350L) for five times continuously, and averaged as the spectral irradiation brightness value of the ROI. Based upon the above process and comparative contrast method [32], the normalized spectral radiance calibration matrix of the system was

obtained, as shown in equation (1):

$$a(\lambda) = \frac{L_{\lambda}}{L_{\lambda_m}} \cdot \frac{1}{\frac{1}{N} \sum_{x=1}^N I(\lambda, x)}, \quad (1)$$

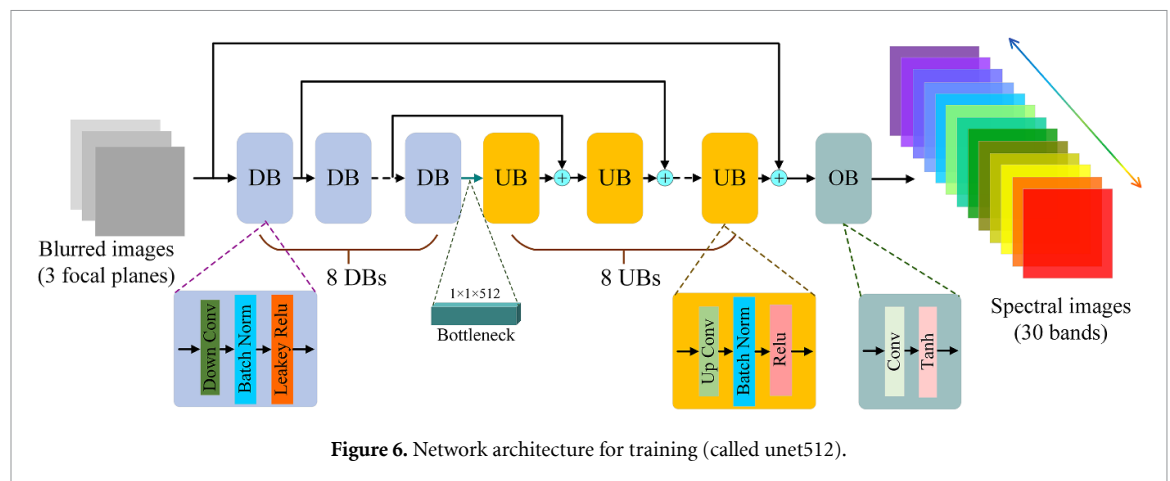
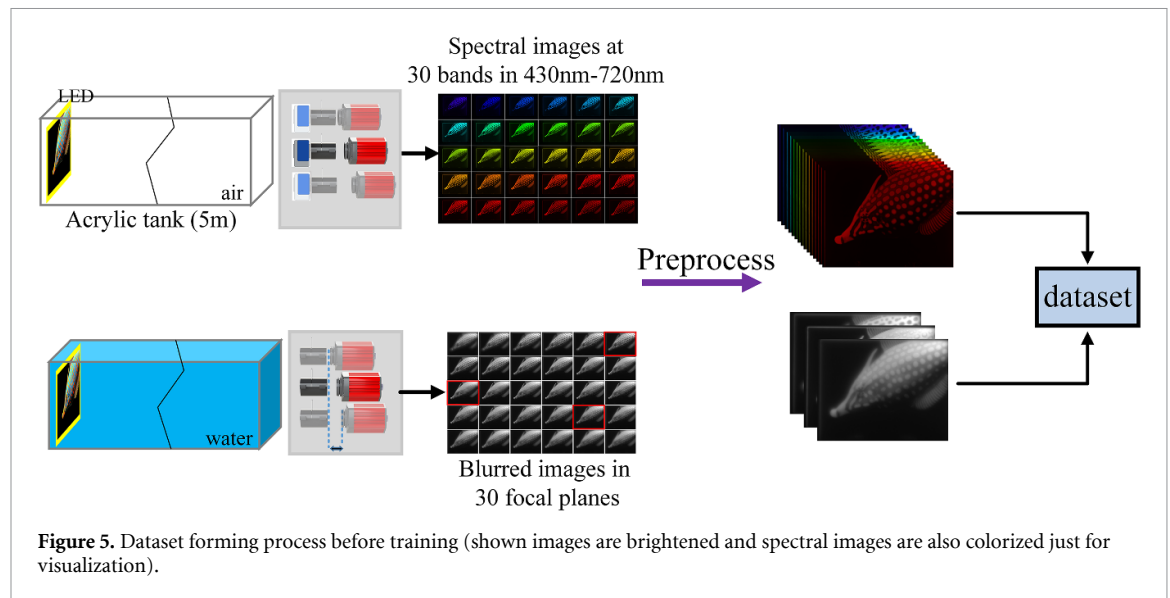
where λ represents wavelength, λ is pixel index in the whiteboard ROI, N denotes the total number of pixels within the region, λ represents the pixel average of the calibrated ROI, λ is the average irradiation brightness value at the ROI of the whiteboard measured by the spectral brightness analyzer and λ denotes the maximum of λ . Once spectral images were obtained, $I(\lambda, x)$ can be determined and the corresponding normalized radiance of each pixel can be calculated using equation (1). This formula was used for the subsequent spectral image conversion from pixel value to normalized spectral radiance in the training process and result visualization part.

3.2. Data acquisition and preprocessing

The method of constructing deep CNN and model training was studied. This method was used for reconstructing hyperspectral images in air from chromatic blur underwater images captured by the proposed imaging system. Therefore, it is necessary to collect a certain amount of sample data through experiments to establish a dataset.

3.2.1. Data acquisition

Some colorful images of high definition were selected and printed upon cardboard paintings to gain 65 targets with size of 44 cm × 35 cm (including a self-designed black and white striped pattern to test the imaging resolution, the dpi value for the printer was 254). As shown in the left half of figure 4, the spectral images in the air and the 65 targets were collected successively by using the imaging system. When collecting spectral images, there was no water in the tank, and LCTF was installed in front of the chromatic blur lens. The LCTF light transmission working wavelength was successively switched from 430 nm to 720 nm with a wavelength step of 10 nm. During this period, the displacement stage was automatically moved to the wavelength focus position according to the chromatic aberration curve, and the spectral images were taken by the sCMOS camera. When collecting the chromatic blur image, the tank was filled with water, the LCTF in front of the lens was removed, the control displacement table was moved to the focus position of each wavelength according to the chromatic aberration curve, and the blur images were taken by the sCMOS camera. In total, 65 sets of chromatic blur-hyperspectral image pairs were captured, each containing 30-band spectral images (430 nm–720 nm, with 10 nm interval), as well as 30 chromatic blur images at the wavelength focus locations. All images captured had a pixel resolution of 560 × 720.



3.2.2. Image registration

Under the chromatic blur imaging system, different incident light wavelengths have various focal lengths. All sets of spectral images and chromatic blur images were taken at different image distances, which resulted in various magnifications. In addition, the image magnification can change by adding LCTE, water media and other factors. The inconsistent magnification can cause image misalignment, making it difficult to accurately calculate meaningful losses between label images and reconstructed images during network training. Therefore, image registration methods were proposed for data pre-processing to deal with the registration problem in spatial relation. A checkerboard calibration plate (mentioned in section 3.1) served as the target. The image coordinates of corner points (where the black squares meet) in the spectral image of 550 nm wavelength were chosen as the benchmark, and the angular points of the remaining spectral images and blur images were changed to make different affine transformations based on the benchmark. These mapping relationships were then applied to all

collected datasets to align the image pairs pixel-to-pixel.

As shown in the right half of figure 5, three frames of chromatic blur images (taking three frames at 480 nm, 550 nm, and 650 nm focus position as examples here) were selected as input, and the 30-band spectral images were paired to form a model dataset for subsequent processing and modeling.

3.3. Model implementation and training

The dataset was divided into two parts: (a) 56 targets for training and validation, and (b) nine targets (including a homemade resolution board) for testing. Among them, the data enhancement method was used for the training set, and the data amount for training was increased to $8\times$. Then, the label spectral image was converted to radiance data by equation (1) for the subsequent modeling.

In order to leverage multi-scale information of the image, this paper expanded on the classic U-net [33] architecture slightly, so that the receptive field of the lowest level feature block of the network included the full image, as shown in figure 6. It features each input

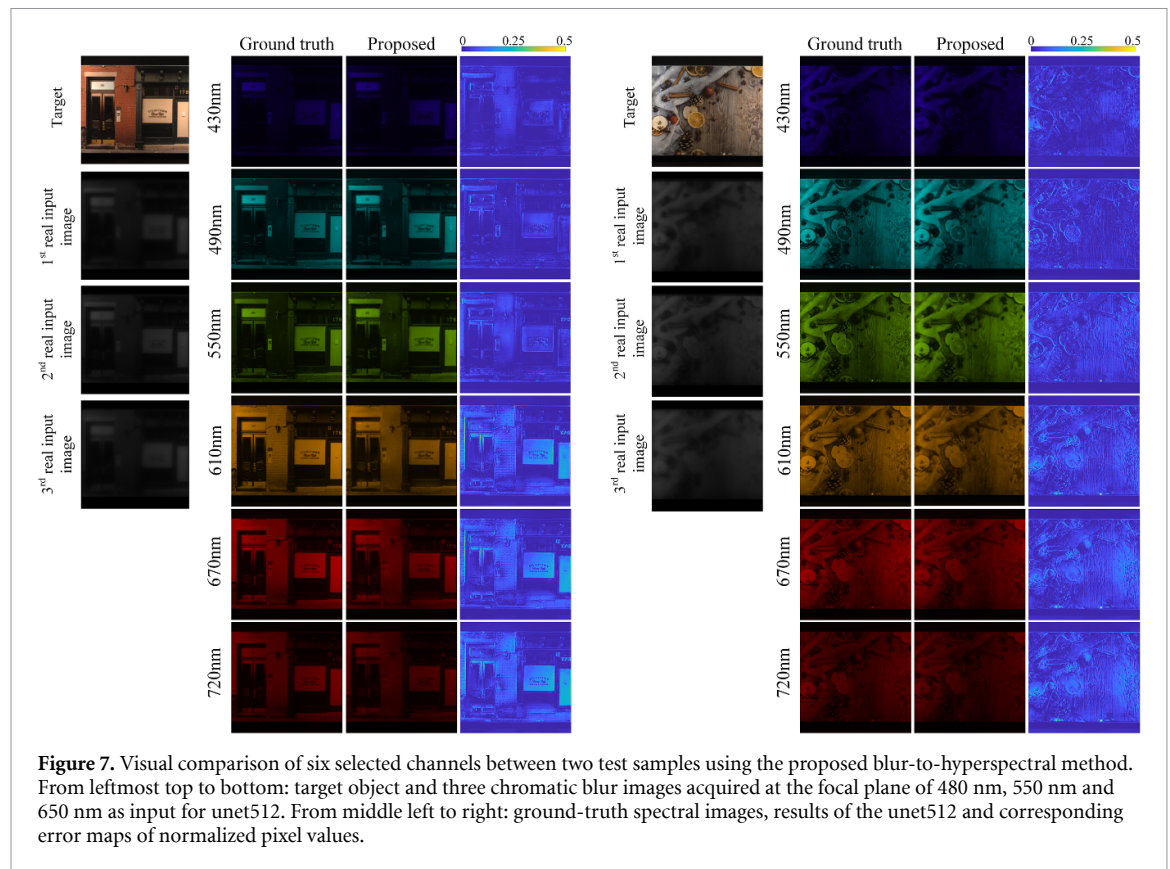


image of 512×512 size with nine size-halved down-sampling operations. In the bottleneck layer, the feature map was reduced to the size of $1 \times 1 \times 512$. After taking the expansion path with nine times of deconvolution up-sampling, the size doubled layer by layer. Finally, the activation function ‘Tanh’ was adopted in the output layer to maintain the distribution of output samples at zero center. The loss function was the mean absolute error to update parameters. Actually, the activation function ‘Tanh’ costs relatively more amount of computing resources. Considering the trade-off between speed and performance, the activation function used in the down-sampling stage was ‘Leaky-Relu’ and ‘Relu’ in the up-sampling stage. The combination effectively enhanced the rate of convergence, and also prevented the network gradient disappearance phenomenon for reconstructing images.

During network training process, input images were centrally cropped at size 512×512 , batch size was set to 1 and Adam optimizer was set to $\beta_1 = 0.9$, $\beta_2 = 0.999$ and $\epsilon = 10^{-8}$. For the adjustment strategy of learning rate, initial learning rate was set to 0.0002, and the piecewise linear decay was implemented, that is, the first 200 epochs keep the initial learning rate, the second set of epochs linearly decay, the learning rate drops to 0 at the last epoch, and the total training epoch number is 890. The network was implemented with PyTorch and trained on a Nvidia Geforce GTX1080Ti graphics processing unit (GPU) with 11 GB video memory.

4. Results and discussion

The reconstruction results are presented and discussed here. Three frames of chromatic blur images of nine test samples were input into the trained network, and the effect of the network model was comprehensively evaluated from the details, resolution, normalized spectral radiance curves and image peak signal-to-noise ratio (PSNR). The spectral image in the data set, namely ground truth (GT), was obtained based on the traditional gaze hyperspectral imaging method. It was used as label in the training stage and GT in the test stage. Therefore, the contrast of the reconstructed spectral image and GT can be regarded as a direct comparison of the effect of visual bionic hyperspectral imaging and conventional gaze hyperspectral imaging mentioned in this paper.

While the underwater chromatic blur imaging has typical blur characteristics, it also has a very obvious low contrast phenomenon. The spectral image reconstruction results of the 1st, 7th, 13th, 19th, 25th and 30th bands of the two test samples were selected for visualization (figure 7). Note that all slices of the reconstructed spectral cube are not displayed here, but only about every fifth is shown, for the purpose of clarity as well as space-saving. The left-most column in the figure shows real images with channels of red, green and blue (RGB) of targets and the three-frame chromatic blur image truly taken by the proposed visual bionic lens as input (obtained at the focus

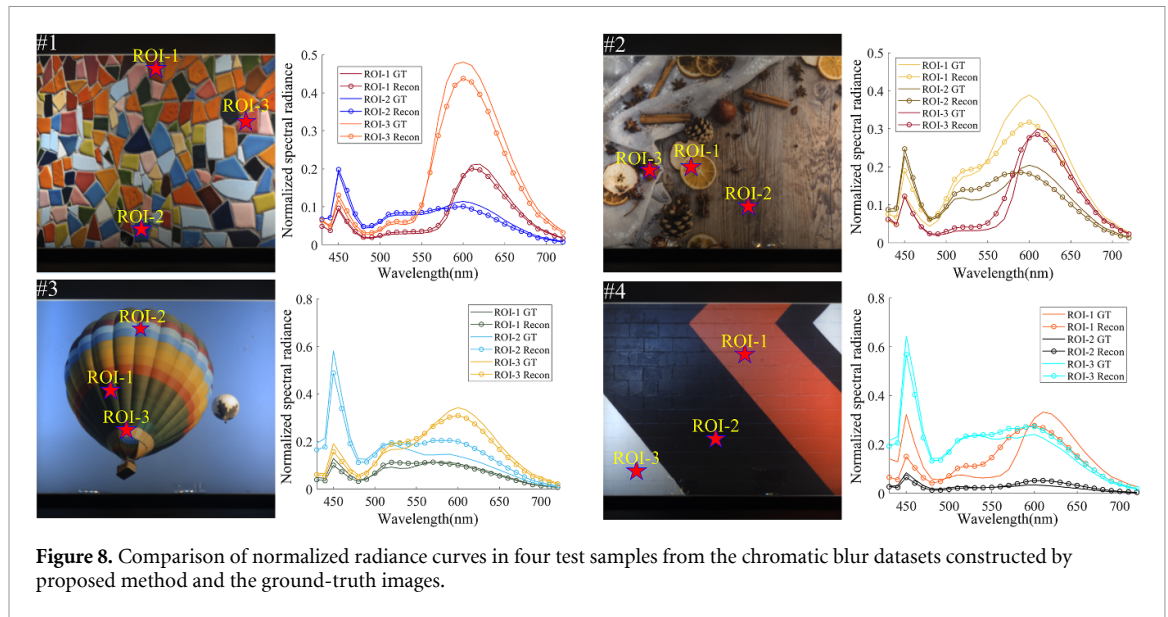


Figure 8. Comparison of normalized radiance curves in four test samples from the chromatic blur datasets constructed by proposed method and the ground-truth images.

Table 1. Deviation evaluation of spectral curve pairs according to figure 8.

NO.	#1			#2			#3			#4		
ROI	1	2	3	1	2	3	1	2	3	1	2	3
RMSE	0.0077	0.0076	0.027	0.039	0.0185	0.019	0.011	0.0389	0.02	0.0668	0.0102	0.0264
ISD	-0.0042	0.0262	-0.0808	-0.0721	0.0196	0.0356	-0.0235	0.0878	-0.0599	-0.0906	0.1119	0.0259
ISSD							0.002					

surface of 480 nm, 550 nm and 650 nm, respectively). It clearly shows that, overall, the reconstructed spectral images performed close to the gaze-captured GT, with better local reconstruction of some flatter dark transitions, or low-frequency regions, compared to regions with high contrast. Due to the certain degree of blur in the input images, CNN method achieved good performance in deconvolution. Compared to conventional gaze spectroscopic imaging, hyperspectral imaging of 30 bands was achieved with a data sampling rate of 10%. In conclusion, the spectral images reconstructed by chromatic blur showed a comparative detail presentation, especially on the contour part, yet only required a low sampling rate.

As mentioned in section 3.1, the pixel values of spectral images were converted into the spoke brightness input network to complete the reconstruction. Accordingly, the normalized radiance curves of part of the test samples and corresponding deviation evaluation of these spectral pairs are compared in figure 8 as well as table 1. Three ROIs marked with five-pointed stars were selected in each scene and the reconstructed irradiation spectrum and gaze imaging of the GT irradiation spectrum were compared. The parameters of RMS error (RMSE) and index of spectrum shifting degree (ISD) [34] represent the deviation between the reconstructed spectrum and GT value in table 1. In addition, the index of system spectrum estimation shifting degree (ISSD) was

also calculated [34] to evaluate the overall performance of the proposed imaging system and reconstruction method. The smaller RMSE is, the closer ISD and ISSD are to 0, indicating better reconstruction and system performances. It can be seen that the system performance was superior in all aspects, which further showed that the method of underwater chromatic blur images has potential for the effective hyperspectral reconstruction of GT.

To verify the spatial resolution of the system, resolution plates of different line pair widths were also added to the test sample that experienced the same reconstruction process. Taking the comparison of 550 nm spectral images as an example (figure 9), the number marked on different line pairs represents the width of black or white lines in cm. The image solution rate was used as the spatial resolution index, that is, the line width (twice the white line and the black line width that can be distinguished at this distance), which is measured in the line pair cm^{-1} (lp cm^{-1}). The band channel map of the reconstructed resolution plate is shown on the left of figure 9, and the spoke brightness of the positive and middle horizontal profile of the image is shown on the right of figure 8. The resolution stripe width of the middle of the picture was 0.3 cm. According to the results, the stripes can be clearly resolved, and the spatial resolution of the system reached 0.3 cm, that is, 1.67 lp cm^{-1} . The mutation

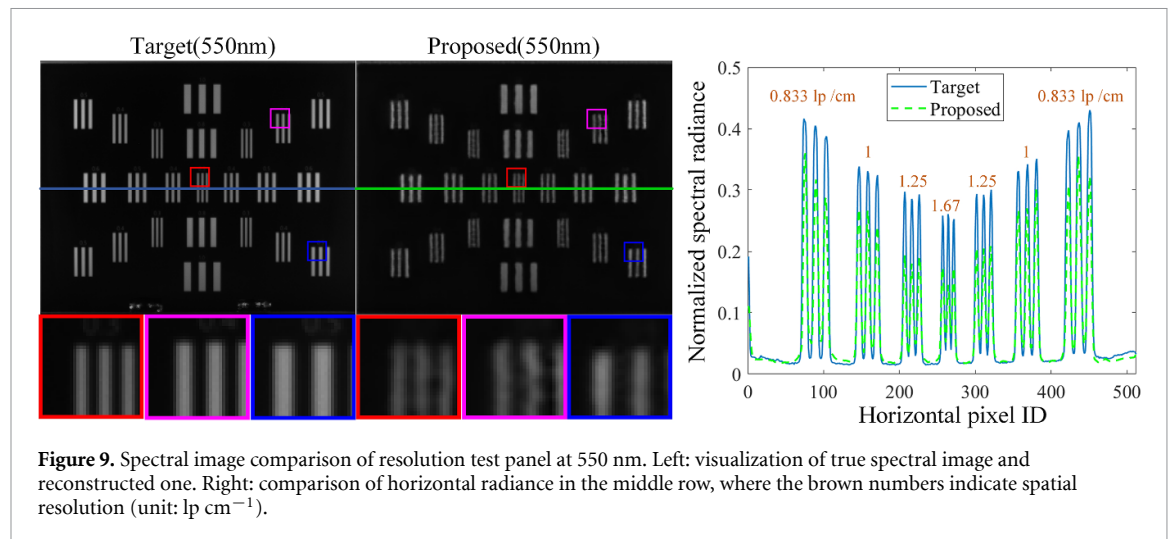


Figure 9. Spectral image comparison of resolution test panel at 550 nm. Left: visualization of true spectral image and reconstructed one. Right: comparison of horizontal radiance in the middle row, where the brown numbers indicate spatial resolution (unit: lp cm^{-1}).

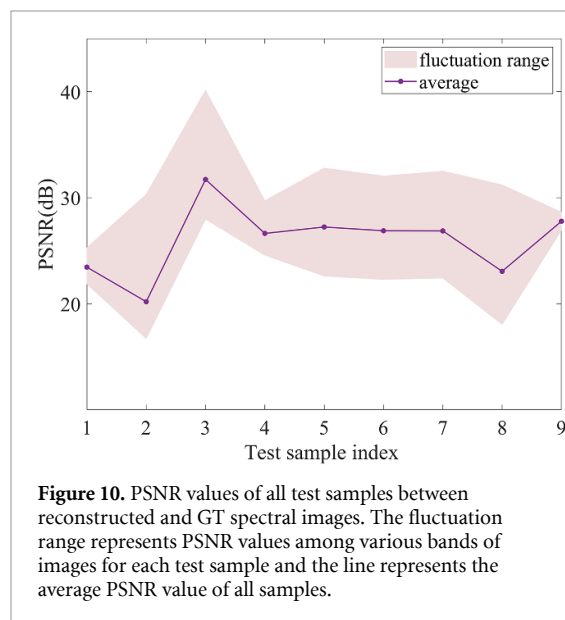


Figure 10. PSNR values of all test samples between reconstructed and GT spectral images. The fluctuation range represents PSNR values among various bands of images for each test sample and the line represents the average PSNR value of all samples.

of each irradiation brightness matched well with the original picture, indicating that the reconstruction effect at the boundary position of the bright line was better.

Figure 10 presents the PSNR results of the reconstructed spectra of all the test samples compared with those of the conventional gaze imaging. The reconstruction stability was measured from among the spectral images of the same band and among the same samples, and it was evaluated by measuring the amplitude of the change. The average PSNR of all test samples remained about 25 dB, with a superior overall performance and a relatively stable reconstruction among different samples.

Traditional gaze hyperspectral imaging is a single wavelength scan in the spectral dimension, which needs LCTF to narrow the input band and costs the sum of required time in each sampling wavelength for imaging. From the perspective of flux amount, compared to the gaze type which needs addition of LCTF for spectral imaging and must consider spectral

transmittance in each band (the transmittance peak of LCTF used in the proposed system does not exceed 70%), chromatic blur imaging system eliminates the use of LCTF, equivalent to accepting 100% transmitted rays in all working bands. Hence, the required exposure time requirement is greatly reduced. If the external factors are ignored, time consumed in the method is the sum of the exposure time in all bands. In the current system, it was equal to the sum of the exposure time of the 30-frame spectral images during the acquisition process, which was approximately 11 082 ms. However, only about 2.1 ms was needed in the bioinspired chromatic blur system, which only required chromatic blur images captured at three bands' focal positions. The specific exposure time of each part is shown in figure 11. In the actual underwater environment, the traditional gaze hyperspectral imager must be static for a long period to complete the imaging, while complex processing methods may be further needed to ensure imaging the same target scene of different bands when meeting with dynamic targets. However, the acquisition method based upon the proposed self-designed chromatic blur lens shown in this paper can obtain a similar reconstruction effect as the traditional gaze imaging, and avoid water interference. The imaging contrast and clarity are similar for both methods, but the required time is shorter.

Undeniably, due to the strong absorption and scattering effect of water on light, optical imaging technology is greatly limited underwater. Therefore, most experiments of underwater UHI systems begin in relatively clear shallow water environment. Similarly, this paper carried out the whole experiment in a self-built underwater environment in the laboratory. The water medium used was plain water, which effectively weakened the blur effect caused by water. Different from common blur, the blur caused by high chromatic aberration plays a positive role in distinguishing light of different wavelengths through regular focal offsets within a certain range according to the

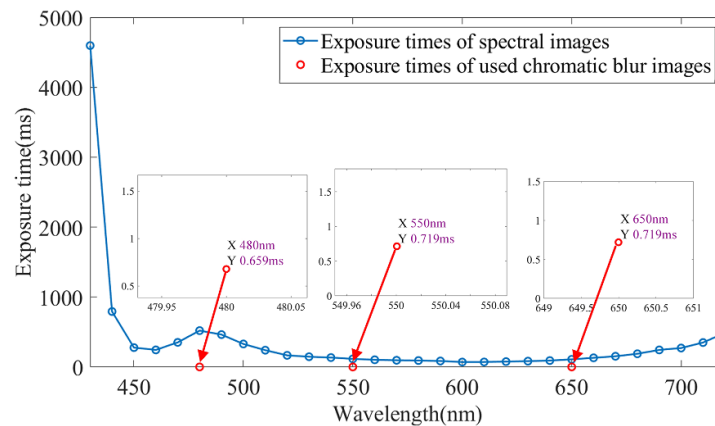


Figure 11. Comparison of acquired exposure time between spectral images and chromatic blur images. Here, the specific exposure times of blur images are magnified and visualized in secondary windows.

squid eye visual system. Hence, this idea was followed in the overall process of data collection. The designed network was also trained in order to study this relation between chromatic blur vision and hyperspectral images. The proposed method showed its latent positive effect of chromatic blur vision in UHI with similar conditions.

5. Conclusion

In this paper, hyperspectral imaging methods and systems based on chromatic blur vision bioinspired mechanism were studied. The imaging principle was inspired by the ocular optometry system of marine cephalopod, and the bionic design of the chromatic blur imaging lens was completed. Finally, a chromatic blur imaging system and underwater target imaging environment were constructed, and the CNN and the model training method were used for the reconstruction of the spectral images. The experimental results showed that only three frames of chromatic blur images were needed to input the trained network, which could satisfactorily reconstruct the spectral images of 30 bands. From the perspective of time consumed to acquire the spectral images by the proposed method and traditional gazing imaging, the present data sampling rate was 10% of the traditional one and the required image acquisition exposure time was only about 2.1 ms. This suggests that the proposed system may be adapted for dynamic detection. In the subsequent research, the engineering packaging design of the proposed system and further network optimization will be implemented, and some application experiments in a variety of practical environmental conditions will be performed. This would further reduce underwater application limits and exploit more potentialities such as dynamic target recognition and mineral classification.

Data availability statement

The data that support the findings of this study are available upon reasonable request from the authors.

Acknowledgments

This work is supported by the Zhejiang Provincial National Science Foundation of China (No. LY19F050016).

ORCID iDs

Tiantian Chen <https://orcid.org/0000-0002-1930-8967>

Jiarui Zhao <https://orcid.org/0000-0001-8267-0670>

Yunzhuo Liu <https://orcid.org/0000-0001-8861-8814>

Shuyue Zhan <https://orcid.org/0000-0002-5961-2402>

References

- [1] Goetz A F 2009 Three decades of hyperspectral remote sensing of the Earth: a personal view *Remote Sens. Environ.* **113** S5–S16
- [2] Dumke I, Nornes S M, Purser A, Marcon Y, Ludvigsen M, Ellefmo S L, Johnsen G and Søreide F 2018 First hyperspectral imaging survey of the deep seafloor: high-resolution mapping of manganese nodules *Remote Sens. Environ.* **209** 19–30
- [3] Kramer S J, Siegel D A, Maritorena S and Catlett D 2022 Modeling surface ocean phytoplankton pigments from hyperspectral remote sensing reflectance on global scales *Remote Sens. Environ.* **270** 112879
- [4] Aggarwal L P and Papay F A 2022 Applications of multispectral and hyperspectral imaging in dermatology *Exp. Dermatol.* **31** 1128–35
- [5] Hadoux X *et al* 2019 Non-invasive *in vivo* hyperspectral imaging of the retina for potential biomarker use in Alzheimer's disease *Nat. Commun.* **10** 1–12
- [6] Abdlaty R, Gobara M, Naiem I and Mokhtar M 2020 Innovative technique for analysis of wastewater

- contaminants using hyperspectral imaging *J. Spectr. Imaging* **9** 1–10
- [7] Jorgensen E J, Kacmarcik A, Prvulovic M and Zajić A 2022 Hyperspectral image recovery via reliability-weighted compressed sensing for hardware Trojan detection *IEEE Access* **10** 96568–12
 - [8] Liu K *et al* 2022 Mapping coastal wetlands using transformer in transformer deep network on China ZY1-02D hyperspectral satellite images *IEEE J. Sel. Top. Appl. Earth Obs. Remote Sens.* **15** 3891–903
 - [9] Wang Z, Xu P, Liu B, Cao Y and Liu Z 2021 Hyperspectral imaging for underwater object detection *Sens. Rev.* **41** 176–91
 - [10] Letnes P A, Hansen I M, Aas L M S, Eide I, Pettersen R and Bytingsvik J 2019 Underwater hyperspectral classification of deep sea corals exposed to 2-methylnaphthalene *PLoS One* **14** e0209960
 - [11] Gilerson A, Carrizo C, Malinowski M, Groetsch P, Foster R and Estrella E H 2019 Multi- and hyperspectral polarimetric imaging of the ocean surface *Proc. SPIE* **11150** 1115007
 - [12] Johnsen G, Ludvigsen M, Sørensen A and Aas L M S 2016 The use of underwater hyperspectral imaging deployed on remotely operated vehicles-methods and applications *IFAC-PapersOnLine* **49** 476–81
 - [13] Bai H, Xue Q, Hao X, Wang Y and Zhang D 2022 Underwater hyperspectral imaging system with dual-scanning mode *Appl. Opt.* **61** 4226–37
 - [14] Dumke I, Ludvigsen M and Ellefmo S L 2019 Underwater hyperspectral imaging using a stationary platform in the trans-Atlantic geotraverse hydrothermal field *IEEE Trans. Geosci. Remote Sens.* **57** 2947–62
 - [15] Xue Q, Tian Z, Yang B, Liang J, Li C, Wang F, and Li Q 2021 Underwater hyperspectral imaging system using a prism-grating-prism structure *Appl. Opt.* **60** 894–900
 - [16] Liu H, Sticklus J, Köser K, Hoving H J T, Song H and Schoening T 2018 TuLUMIS-a tunable LED-based underwater multispectral imaging system *Opt. Express* **26** 7811–28
 - [17] Song H, Mehdi S R, Wu C, Li Z, Gong H, Ali A and Huang H 2021 Underwater spectral imaging system based on liquid crystal tunable filter *J. Mar. Sci. Eng.* **9** 1206
 - [18] Brown P K and Brown P S 1958 Visual pigments of the octopus and cuttlefish *Nature* **182** 1288–90
 - [19] Mäthger L M, Barbosa A, Miner S and Hanlon R T 2006 Color blindness and contrast perception in cuttlefish (*Sepia officinalis*) determined by a visual sensorimotor assay *Vis. Res.* **46** 1746–53
 - [20] Douglas R H 2018 The pupillary light responses of animals; a review of their distribution, dynamics, mechanisms and functions *Prog. Retin. Eye Res.* **66** 17–48
 - [21] Chubb C, Chiao C C, Ulmer K, Buresch K, Birk M A and Hanlon R T 2018 Dark scene elements strongly influence cuttlefish camouflage responses in visually cluttered environments *Vis. Res.* **149** 86–101
 - [22] Jagger W S and Sands P J 1999 A wide-angle gradient index optical model of the crystalline lens and eye of the octopus *Vis. Res.* **39** 2841–52
 - [23] Hanke F D and Kelber A 2020 The eye of the common octopus (*Octopus vulgaris*) *Front. Physiol.* **10** 1637
 - [24] Stubbs A L and Stubbs C W 2016 Spectral discrimination in color blind animals via chromatic aberration and pupil shape *Proc. Natl Acad. Sci.* **113** 8206–11
 - [25] Zhan S, Zhou W, Ma X and Huang H 2019 Hyperspectral imaging bioinspired by chromatic blur vision in color blind animals *Photonics* **6** 91
 - [26] Zhan S, Liu Y, Ma X, Zhou W and Huang H 2020 Spectral discrimination and spatial resolution from retinal chromatic blur images in color blind animals *Spectrosc. Lett.* **53** 349–59
 - [27] Jin K H, McCann M T, Froustey E and Unser M 2017 Deep convolutional neural network for inverse problems in imaging *IEEE Trans. Image Process.* **26** 4509–22
 - [28] Lim B, Son S, Kim H, Nah S and Mu Lee K 2017 Enhanced deep residual networks for single image super-resolution *USA IEEE Conf. on Computer Vision and Pattern Recognition Workshops (CVPRW)* pp 136–44
 - [29] Fu H, Bian L, Cao X and Zhang J 2020 Hyperspectral imaging from a raw mosaic image with end-to-end learning *Opt. Express* **28** 314–24
 - [30] Zhou C and Wang Z 2018 Mid-frequency MTF compensation of optical sparse aperture system *Opt. Express* **26** 6973–92
 - [31] Chen R, Zheng Z and Pan J 2021 Fast blind deblurring of QR code images based on adaptive scale control *Mobile Netw. Appl.* **26** 2472–87
 - [32] Nguyen R M, Prasad D K and Brown M S 2014 Training-based spectral reconstruction from a single RGB image *In Proc. of the European Conference on Computer Vision (ECCV) (Switzerland)* pp 186–201
 - [33] Ronneberger O, Fischer P and Brox T 2015 U-net: convolutional networks for biomedical image segmentation *Germany Int. Conf. on Medical Image Computing and Computer-Assisted Intervention (MICCAI)* pp 234–41
 - [34] Li S, Liao N and Sun Y 2007 A new parameter for evaluating spectral estimation precision of multispectral camera *Spectrosc. Spectral Anal.* **27** 1461–4